

# A Family of Full Spacecraft-to-Payload Isolators

**Allen J. Bronowicki and John W. Innis**

*Northrop Grumman Space Technology*

*Upcoming space payloads require alignment between optical elements on the order of a few nanometers and pointing tolerances of milliarcseconds.*

*Examples from the National Aeronautics and Space Administration's Origins program are the James Webb Space Telescope (JWST) and the Space Interferometry Mission (SIM). Northrop Grumman Space Technology has developed a dual-stage vibration isolation approach that attenuates spacecraft-induced vibrations by three to four orders of magnitude. The second stage is an isolator placed between the spacecraft bus and the optical payload. The isolator consists of a set of passively damped, flexured beams. The isolators employ techniques for embedding viscoelastic damping layers within composite lay-ups that were pioneered and patented by Northrop Grumman Space Technology.*

*Unit development transfer-function test results for the isolator beams are presented. The tests show excellent correlation with analytic models. An efficient analysis technique was developed that combines the standard finite-element method with closed-form solutions for damping treatments and fractional-derivative models of viscoelastic material behavior.*

*System tests for the SIM isolator were conducted on an interferometer testbed with realistic, complex dynamics. System tests for the JWST isolator were performed with a 1000-kg full telescope mass and inertia simulator. Both tests met performance goals and corresponded well with analytic predictions.*

## Introduction

As we develop succeeding generations of astronomical telescopes, the engineering challenges become ever more difficult. Northrop Grumman is striving to build systems that are larger, colder, and more precise. Here we describe a solution to vibration control challenges on two missions in the National Aeronautics and Space Administration's Origins program—the James Webb Space Telescope (JWST) and the Space Interferometry Mission (SIM). Northrop Grumman Space Technology is the prime contractor for the JWST Observatory (Figure 1), being developed for Goddard Space Flight Center. We are the spacecraft industry partner on SIM (Figure 2), where the Jet Propulsion Laboratory (JPL) is prime. On both programs, we provide both the spacecraft life support systems and the primary structures, in addition to maintaining a benign thermal environment and a stable platform.

To capture sufficient photons emitted from the first (oldest) and farthest galaxies, the JWST will have a primary mirror aperture of 6.5 m, 2.7 times greater than its predecessor, the Hubble Space Telescope. To achieve such a large size, the mirror support structure is deployable and inherently flexible. Telescope modes on JWST are in the range of 7 Hz for the secondary mirror and 11 Hz for the primary mirror, whereas comparable frequencies on Hubble were five times higher.

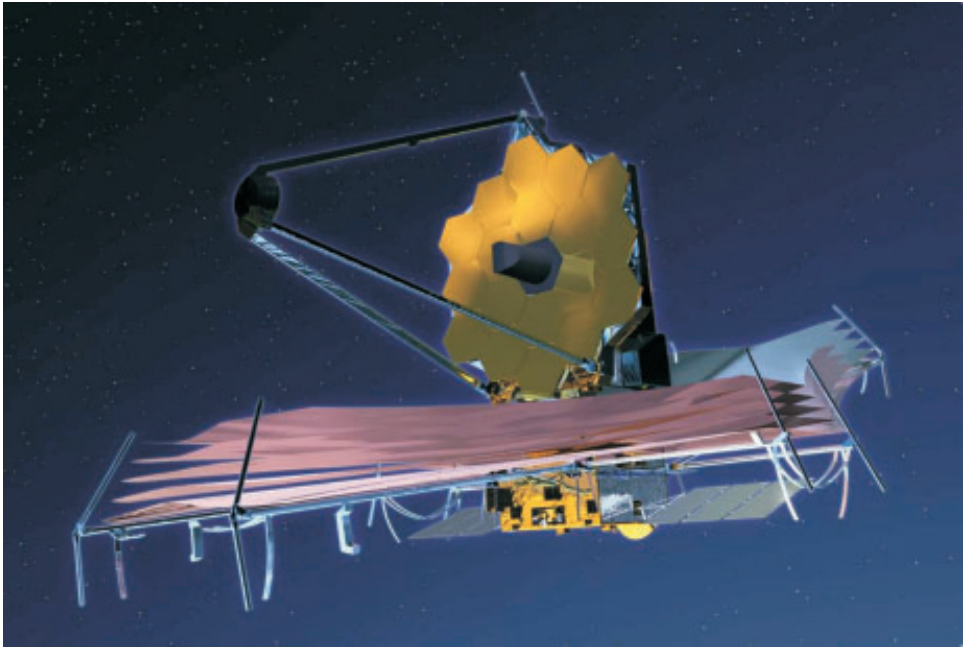


**Figure 1. Deployed James Webb Space Telescope Observatory**

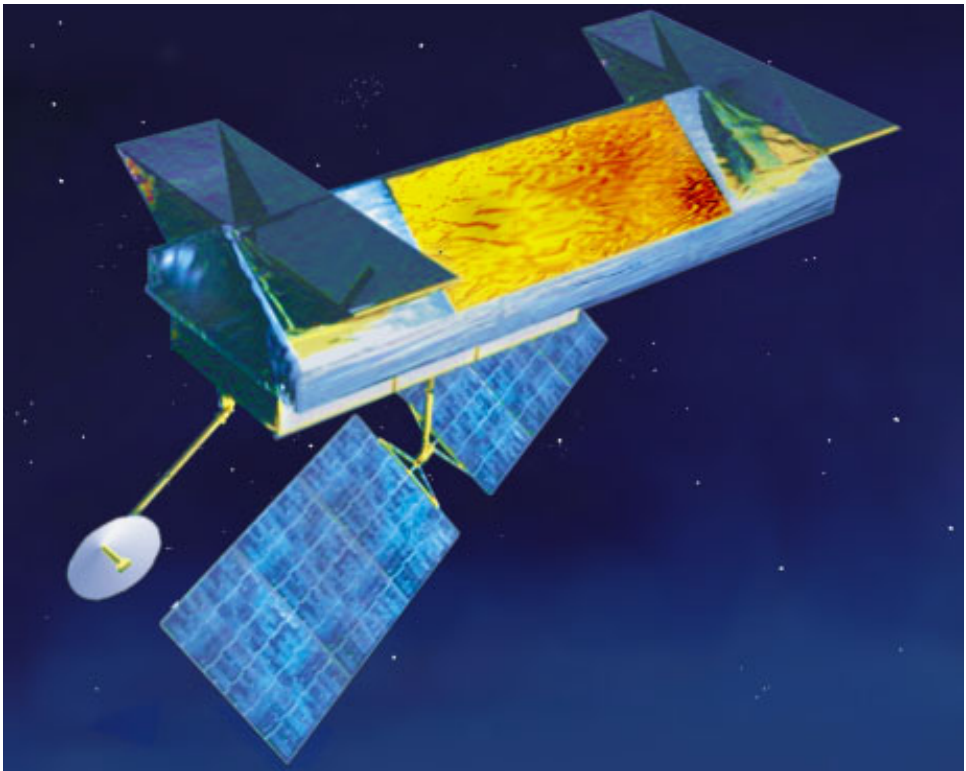


**Figure 2. Space Interferometer Mission flight vehicle**

Since the first galaxies are receding from us rapidly, light emitted in visible wavelengths is stretched into infrared wavelengths as it reaches our solar system. To capture such infrared images without jamming itself with thermal self-emission, the JWST telescope must operate at an average temperature of 40 K (–460°F below room temperature). Typical vibration-damping treatments, such as fluid or viscoelastic dampers, would rigidify in such frigid conditions. Thus, vibration control must rely heavily on vibration isolation, more so than on stiffness or damping, as explained in a sidebar, “What Is Vibration Isolation?” (pages 24–25).

JWST will correct for drifts in mirror positions using adaptive optics, but only at intervals of days or weeks. Vibrations of the 18 primary mirror segments must therefore remain below 10 nm without help from active correction. Such alignment accuracy is required to maintain planar wavefronts as starlight reaches the focal plane. Pointing errors induced by vibration must remain below 4 milliarcseconds (mas) [1] to maintain starlight well within individual pixels on the imaging camera.

SIM employs an astrometric instrument that will measure the angular separation between stars to an accuracy of a few microarcseconds [2]. Such precision will enable, for instance, the indirect detection of planets orbiting nearby stars by measuring the gravity-induced wobble in the star’s position. SIM will combine and interfere starlight using pairs of small, 15-in.-aperture siderostats separated at opposite ends of a 10-m optical bench. The relative path lengths to the star along the two arms of the interferometer are measured to an accuracy of a few picometers using precise laser gauges. Using simple trigonometry, the angles between the stars can be inferred.

The SIM project is organized along two themes:

- The role of the *nano group* is to control the motions of optical elements to a precision of a few nanometers. Northrop Grumman’s work in providing the stable platform falls within the nano group’s charter.
- The *pico group* must then measure internal and stellar path lengths to the required picometer accuracy.

For SIM, the stars being measured will usually be close enough that photon flux is sufficient to allow active stabilization of optical path lengths. So, below about 10 Hz, mirror positions are corrected actively. Above 10 Hz, however, mirror motions must be limited by the vibration control system to a 10-nm requirement.

Both the SIM and the JWST programs have adopted similar dual-stage vibration isolation strategies. In the science mode, all nonessential vibration-causing mechanisms or thrusters will be inactive. Devices that must operate during science are confined to the spacecraft compartment and placed on individual vibration isolators. Such source isolation constitutes the first isolation stage. The reaction wheels must operate continuously to orient the instrument and will generate imbalance forces at multiples of their spin rate. JWST also will have a cryocooler to maintain the Mid InfraRed Instrument’s focal plane at 6 K. The compressor generates pulsating forces at harmonics of the 30-stroke-per-second drive speed. Reaction wheels and compressor are placed on passive isolators having a roughly 10-Hz break frequency with about 5% damping.

The second isolation stage comprises an isolator placed between the spacecraft compartment and the optical payload. JWST and SIM will be the first missions to completely isolate a spacecraft in that way. With no active control, JWST requires an extremely soft 1-Hz spacecraft isolator. SIM can, however, employ a more easily realized 5-Hz isolator,

## What Is Vibration Isolation?

Three tools can be used in designing a low-vibration structure: stiffness, damping, and isolation. In spacecraft design, we enhance *stiffness* by using materials with a high ratio of elastic modulus to density, such as graphite composites. Structural optimization then finds the best distribution of structural material. Stiffness reduces response by giving lower deflections for unit applied force.

*Damping* reduces response at a structure's natural frequency by removing energy from each cycle of response as the structure resonates. A damping material will provide a component of restoring force 90° out of phase with the input displacement.

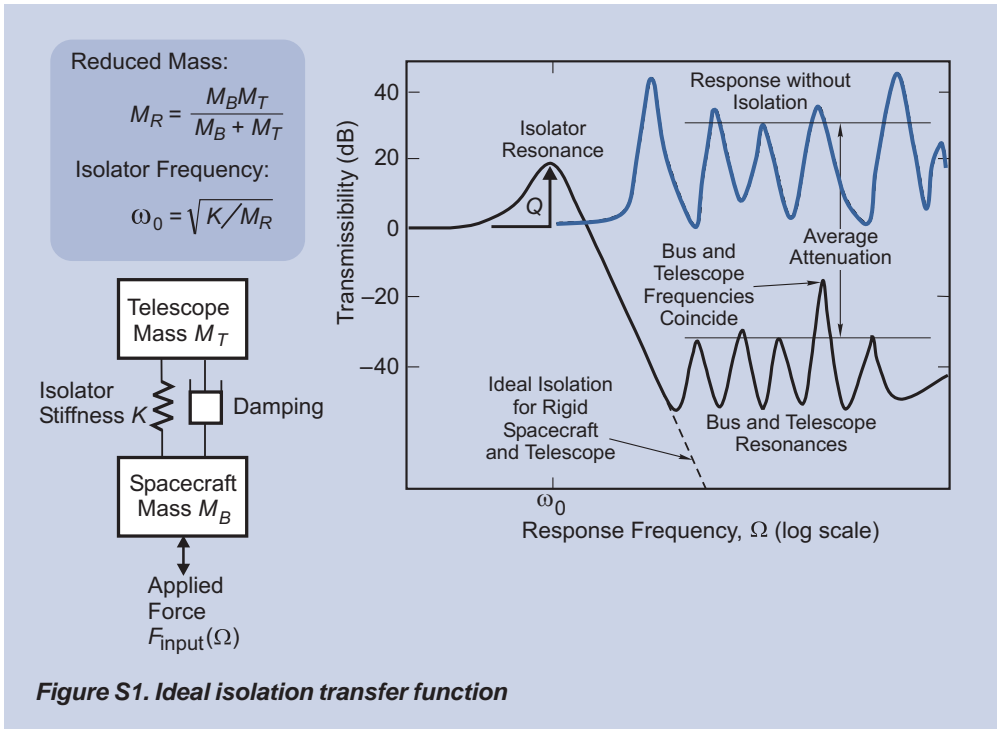
*Vibration isolation* provides a compliant separation between a payload and a vibrating body—in our case, the spacecraft bus. The soft interface means that the bus can vibrate, but the transmitted force is low. The ideal form of this force is

$$F_{\text{transmitted}} = \frac{F_{\text{input}}}{1 - \left(\Omega/\omega_0\right)^2 + i2\zeta\left(\Omega/\omega_0\right)},$$

where  $\omega_0$  is the isolator natural frequency,  $\Omega$  is the response frequency, and  $\zeta$  is the damping coefficient.

Transmissibility peaks at the isolator natural frequency ( $\Omega = \omega_0$ ), as shown in Figure S1. The amplitude of the peak is  $Q = 1/(2\zeta)$ , which we reduce by introducing damping into the isolator. At higher response frequencies ( $\Omega > \omega_0$ ), the transmissibility rolls off as  $1/\Omega^2$ . Physically, the roll-off is due to the force being absorbed as an inertial load by the forced body, whereas displacement is proportional to the inverse square of acceleration. The rolloff does not continue forever, since the ideal isolation curve applies only to rigid bodies. The attenuation ceases to improve when the bodies on either side of the isolator start to exhibit their own resonances, and the rigid masses “break up.” Even so, vibration response is much lower with the isolator than without.

As shown in the figure, the isolator has a  $Q$  of about 10 (5% damping) at its resonant frequency. In the higher-frequency isolation band, however, an attenuation of two or more orders of magnitude is exhibited, comparing the isolated dynamics to the unisolated. A vibration isolator typically works best with damping levels as shown, since higher damping can result in increased transmission through the viscous element at high frequency.



since active control augments the isolator below 10 Hz. Simulations on both JWST and SIM have shown that, if one relied on source isolation alone—hard-mounting the spacecraft to the optical payload—vibration allocations would be exceeded by two orders of magnitude or more.

This article first describes the spacecraft isolator configurations for both missions and then details the design and analysis of an individual isolator strut. Unit vibration tests of the isolator struts are described and compared with model predictions. Results of system-level tests for both missions are presented. Finally, we discuss the possible extension of the beam isolator concepts to future missions using active-structure technology.

## Beam Isolator Configuration

For both missions, the spacecraft isolator consists of a set of simple tubular beams with constrained-layer viscoelastic damping. The end of each beam has a titanium V-flexure that transmits lateral forces through the beams but releases axial forces. The arrangement is analogous to leaf-spring suspensions on early automobiles.

For JWST, a set of four 52-in.-long graphite beams is employed, achieving 1-Hz isolation in the bounce (Z) direction [3], as Figure 3 shows. Each beam clamps to a deployable tower that provides thermal isolation between the cryogenic optical payload and a multilayer sunshield placed atop the spacecraft. Four struts are used to obtain as wide as possible a footprint on top of the spacecraft, which measures about 100 in. square.

Maximizing the footprint enables control of rocking motions—critical because both the payload and the spacecraft/sunshield have very large inertias. In fact, the sunshield dimensions compare with those of a tennis court. Thus, when deployed, the JWST isolator will be by far the largest vibration isolator in space. It is so large and soft that a

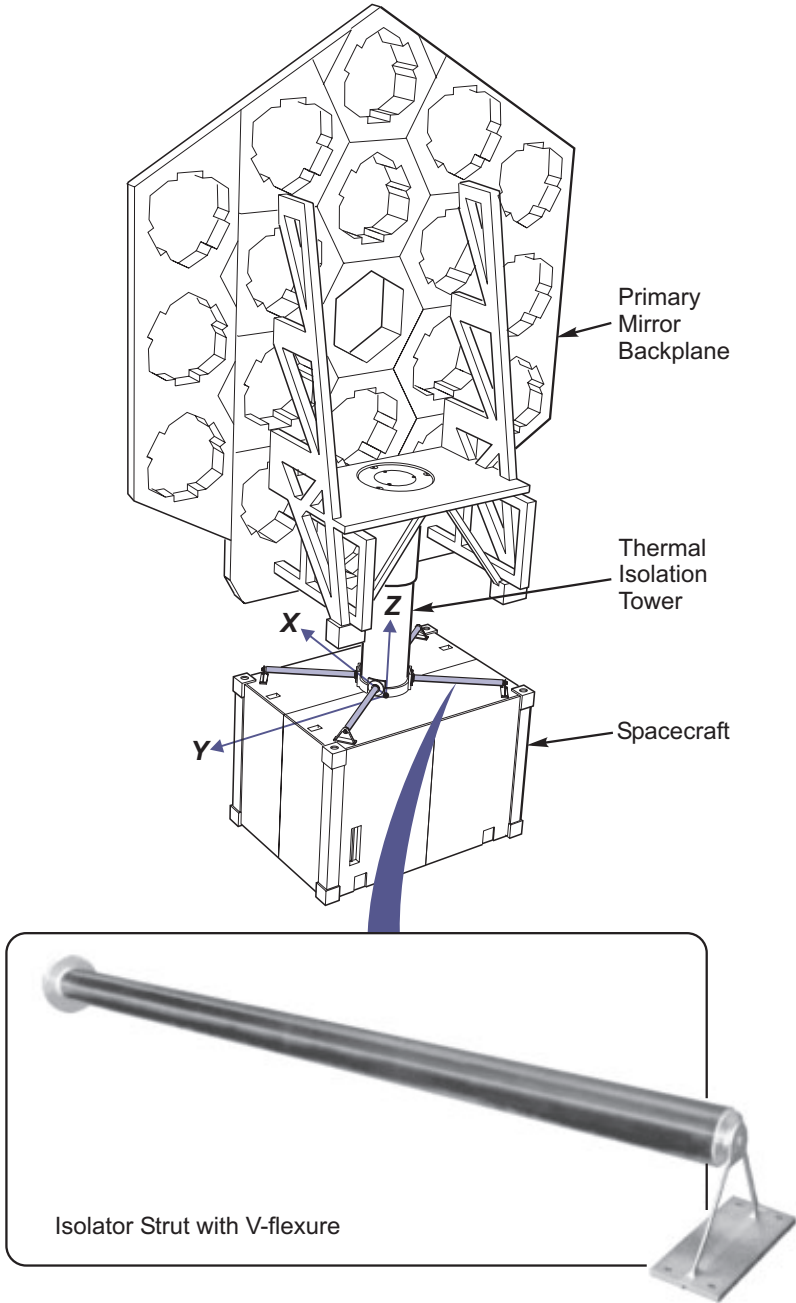


**Figure 3. Layout of Webb telescope spacecraft isolator**

gravity-offload system is required for ground testing. The JWST isolator struts are also the first stage in thermal control of the telescope. They are controlled to a temperature of 0°C, being cold-biased by the thermal isolation tower.

The SIM configuration has all spacecraft equipment contained in a “backpack,” which is then isolated from the Precision Support Structure (PSS) holding the interferometric payload. System Testbed 3 (STB3), shown in Figure 4a, was developed by Northrop Grumman and installed at JPL to demonstrate passive isolation and active path-length control on a full-scale, dynamically rich structure. The 9-m-long STB3 PSS is suspended on three 0.4-Hz nano-K™ passive-suspension devices that simulate the gravity-free conditions of space. A 5-Hz isolator operates in conjunction with the active path-length control, which rejects low-frequency vibrations [4,5]. The backpack isolator consists of three 24-in.-long fiberglass struts. The base of each strut is fixed to the top of the backpack, and the V-flexure is attached to the bottom of the PSS, as Figure 4b shows.

Fiberglass was chosen because it has a very high strain to failure, allowing the backpack isolator to be tested in gravity without an offload system. In fact, we attempted to proof-load one of the STB3 struts to destruction. The strut was loaded to 1000 lb, more than six times its design-limit load. The strut deflected just 3 in. laterally and recovered fully with no damage.

## Isolator Strut Design and Analysis

A cross section through a typical isolator strut is shown in Figure 5. The construction consists of an inner tube having a 2.5-in. inner diameter, covered with a layer of soft viscoelastic damping material (VEM), overwrapped with a graphite constraining layer segmented at a spacing of  $L_c \sim 8\text{--}10$  in. As depicted in Figure 5, segmentation forces axial stress in the inner tube to weave through shear stress in the damping layer into axial stress in the constraining layer, and then back to the inner tube. Strain energy deposited in the lossy VEM is thus maximized, allowing for maximal dissipation of vibrational energy. An optimal segmentation length exists for each given construction, operating temperature, and frequency. Since frequencies of the fundamental isolator mode and local bending modes of the beam are widely separated, a compromise segmentation length is chosen.

The analysis of a structure having viscoelastic constituents is difficult because VEM properties are both temperature- and frequency-dependent, whereas typical finite-element method (FEM) codes operate best when properties are constant. We addressed that problem by developing an efficient analysis technique, hybridizing the traditional FEM with complex frequency-domain analysis. The FEM supplies a set of basis functions derived from real normal mode shapes computed using a set of constant, nominal properties. The basis functions are recombined in a postprocessing step to reflect the actual operating temperature and frequency. The process is summarized in the flowchart of Figure 6 and described below.

**Viscoelastic Material Model.** The viscoelastic material employed is the acrylic polymer 3M™ Scotchdamp™. At low temperatures, or equivalently at high frequencies, the material is stiff (glassy region). Conversely, at high temperatures or low frequencies, the material is soft (rubbery region). The transition region in between is where maximal damping occurs. Unfortunately, the rate of change of stiffness is also the greatest in the transition region, so achieving an optimal strain energy balance between base structure, VEM, and constraint is difficult.

a. Structure and suspension

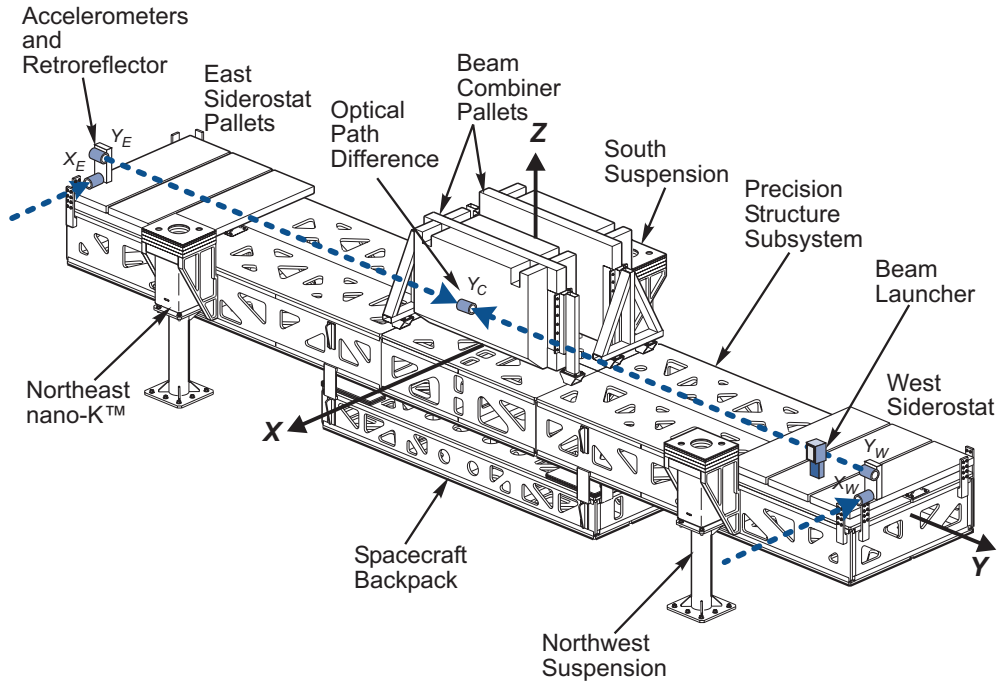


**Figure 4. SIM System Testbed 3**

One feature that simplifies our analysis is the VEM’s “thermo-rheologically simple” behavior: a correspondence exists between frequency and temperature, so a single curve can be used to describe both dependencies. The formula for the reduced frequency  $f_r$  as a function of absolute temperature  $T$  is  $f_r(T) = \alpha(T)f$ , where  $\alpha(T)$  is a temperature-shift function and  $f$  is the actual response frequency.

The complex shear modulus  $\tilde{G}(f_r)$  is used to model the amplitude and phase properties of the VEM. Storage modulus  $G$  is the real part of complex modulus, and loss factor  $\eta$  is the ratio of imaginary and real parts, i.e.,  $\tilde{G} = G(f_r)[1 + j\eta(f_r)]$ . The phase angle of stress in the VEM with respect to strain is  $\tan^{-1} \eta$ . An effective VEM has a loss factor around 1, so the restoring force lags about  $45^\circ$  behind displacement. Performing structural calculations using complex variables is a compact means of accounting for stiffness and damping properties simultaneously [6].

The final simplification in the VEM model is the use of fractional derivatives [7]. Force in an elastic material is proportional to displacement. Force in a viscous material is proportional to velocity, the first time derivative of displacement. The behavior of viscoelastic materials is intermediate and thus proportional to a fractional time derivative of displacement. The order of the fractional derivative  $\beta$  is usually in the vicinity of one-half. For the Scottdamp material,  $\beta$  is 0.6. Using a fractional derivative model, one can obtain an excellent representation of complex modulus behavior over many decades of reduced frequency with just four parameters:

- A low-frequency stiffness asymptote  $G_0$

b. Close-up of backpack and isolator struts

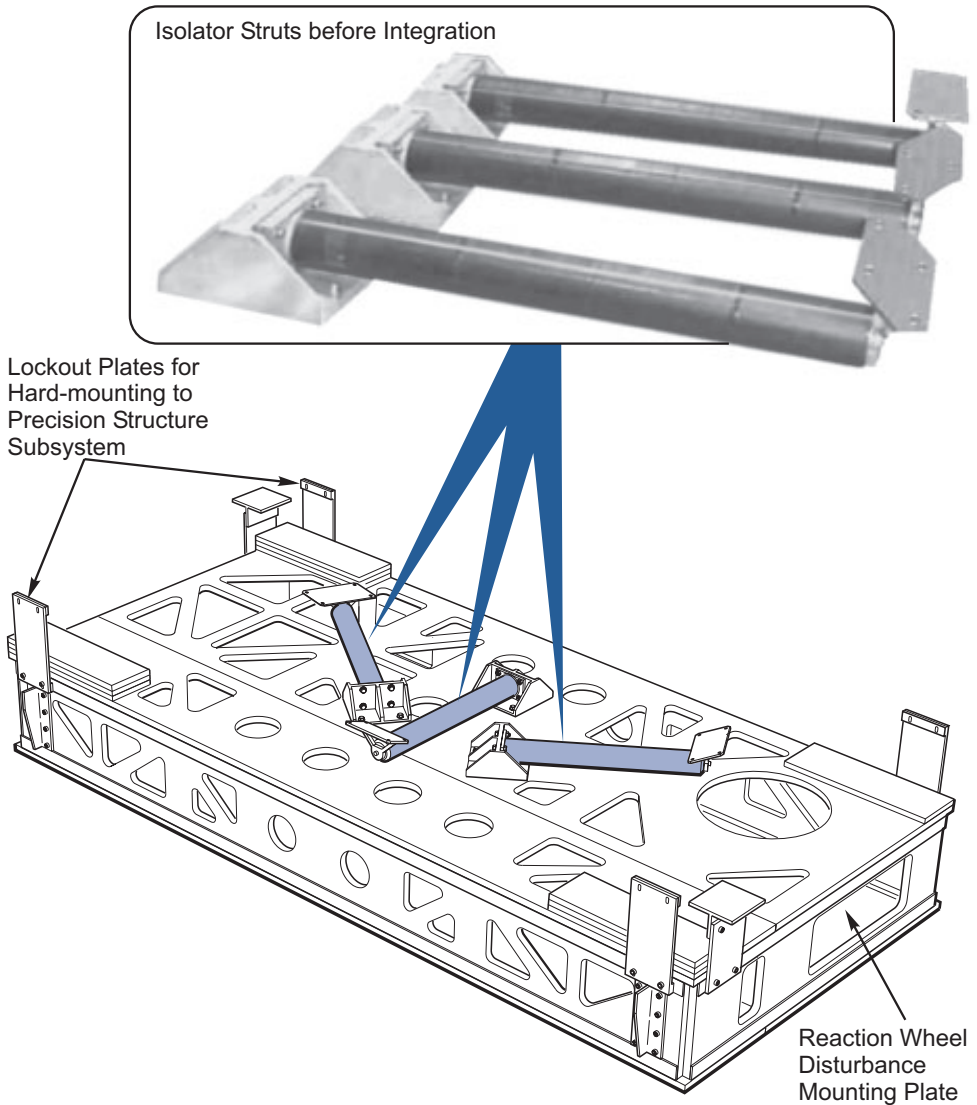


**Figure 4. Concluded**

- Zero and pole frequencies  $a$  and  $b$ , which respectively define the beginning and end of the transition region
- The slope  $\beta$

Figure 7 compares measured data points for Scottdamp’s storage and loss factor with curves defined by the fractional derivative model.

**Segmented Constraint Model.** A closed-form solution can be obtained for the response of a segmented constraint floating on an elastic base structure and a viscoelastic layer [8]. The solution involves first-order differential equations for axial strain in the base layer and the constraining layer, coupled by shear stress in the VEM layer. The shear strain is determined by the difference in axial displacement between the two layers sandwiching

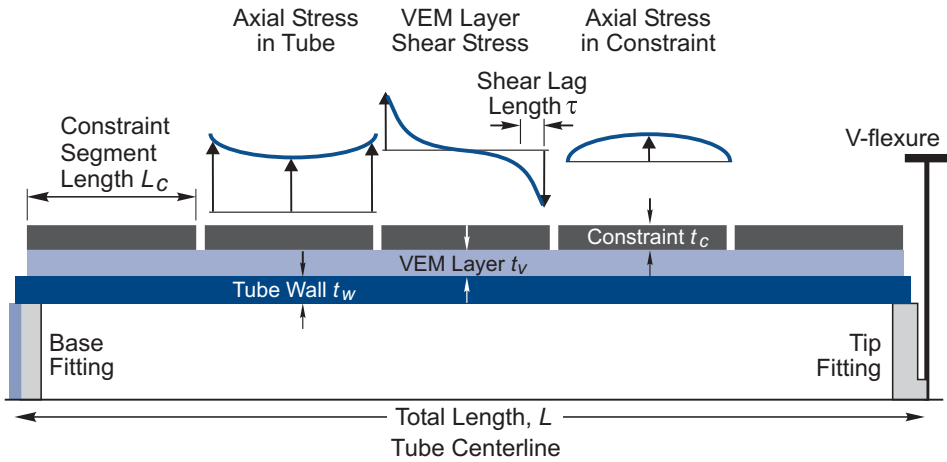


**Figure 5. Cross section of typical isolator strut**

the VEM. The solution provides the shear lag length  $\tau$ , which is the distance required to transfer the axial force from the inner tube to the outer tube (see Figure 5).

When the tube stretches, the constraint will stretch only by the action of the VEM. Figure 5 demonstrates that the VEM shear stress peaks at both ends of the constraining layer, while the axial stress in the tube decreases away from the ends, and the axial stress in the constraint increases away from the ends. Thus, axial load is being transferred from the tube to the constraint by shearing the VEM. Segmenting the constraint creates several opportunities for the load transfer to take place on an individual tube. That way, we maximize energy absorption into the VEM.

The solution is obtained from the relative stiffnesses of the inner tube wall,  $k_w = Et_w$ ; the VEM,  $k_v(f_R) = \tilde{G}(f_R)/t_v$ ; and the constraint,  $k_c = Et_c$ ; where  $E$  is the axial modulus and  $t$  is layer thickness. Note that decreasing the thickness of the VEM layer increases its stiffness. The complex stiffness  $\tilde{k}(f_R)$  of the tube wall/VEM/constraint system is obtained, as shown in Figure 6. For design purposes, it has been shown that damping is maximized when  $\tau$  is one-third the length  $L_c$  of the constraint segment.

Model predictions for the loss factor in the JWST isolator struts are shown in Figure 8 for a range of operating temperatures and frequencies. For JWST struts, the constraint segment length was  $L_c = 9.55$  in. The predicted damping maximizes at a loss factor of  $\eta = 0.135$ , or a damping ratio of  $\zeta = \eta/2 = 6.75\%$ . The thermo-rheologically simple behavior is evident in the curves presented in Figure 8, in that the different temperature curves can be translated laterally on the frequency axis to give identical behavior. One peak is seen to occur at the nominal JWST operating conditions of  $T = 0^\circ\text{C}$  and  $f = 1$  Hz.

**System Analysis.** Real normal modes of the JWST are computed using a Nastran (originally, NAsa STRuctural ANalysis) finite-element model, which discretizes structural response using a set of assumed shape functions that approximate the strain state of the body. A set of constant stiffness and loss factor properties are used for a single assumed temperature and frequency. The natural frequencies of vibration and their corresponding mode shapes and damping ratios are saved for this nominal property set.

A frequency-domain solution is then performed for the actual operating temperature. Actual complex stiffness is determined at each operating frequency and temperature, as

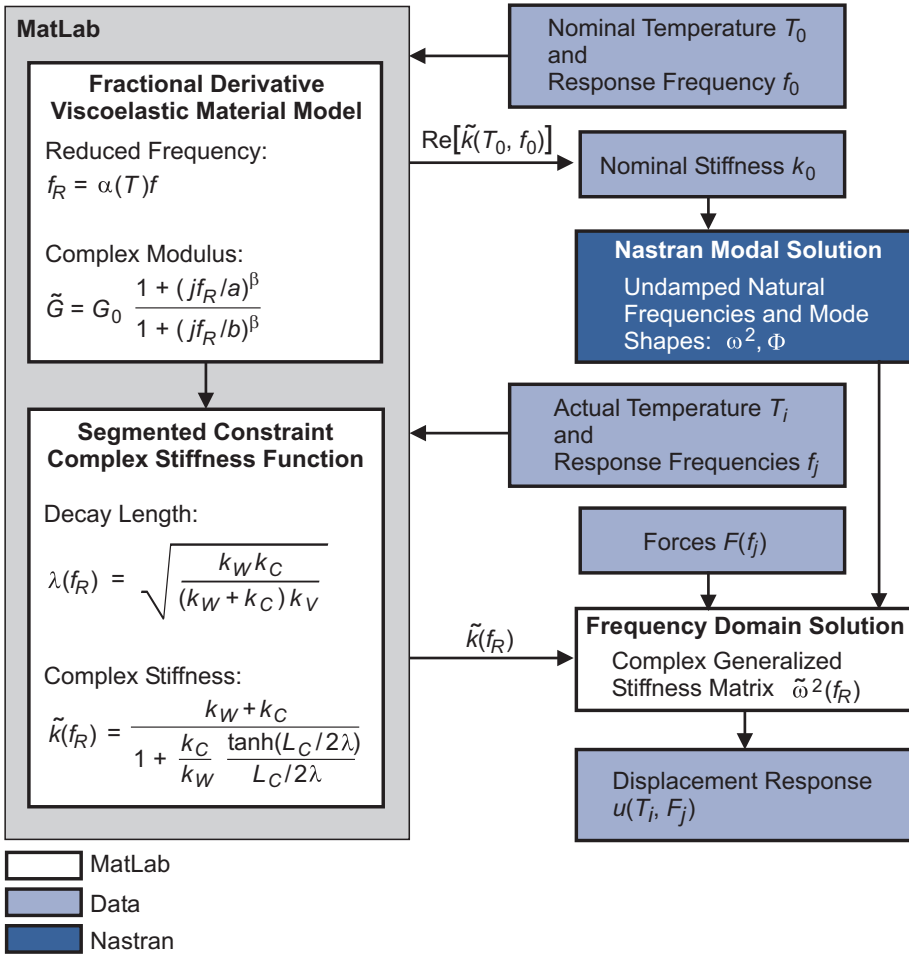


**Figure 6. Analysis of damped structures with viscoelastic constituents**

Figure 6 shows, allowing formation of a complex generalized modal stiffness matrix  $\tilde{\omega}^2$ . By inverting the matrix, a displacement response for a given force input occurs at each frequency. The natural frequencies and damping ratios are found by computing the complex eigenvalues of  $\tilde{\omega}^2$  evaluated at the frequency of each resonant peak.

## Unit Isolator Strut Transmissibility Tests

Transmissibility measurements were performed on individual isolator struts to confirm isolation performance and model predictions. A 147-lb mass simulator was suspended from the laboratory ceiling on a high-strength string (the largest mass we felt comfortable with in the laboratory setting). The test mass achieved a 5.6-Hz lateral frequency for the SIM/STB3 struts, close to the desired 5-Hz operational frequency. For the JWST struts, a 2-Hz lateral mode was achieved. That was sufficient for model-matching purposes, but not to demonstrate operation of a 1-Hz isolator. Operation at 1 Hz was demonstrated later in the system modal survey, as described in the following section.

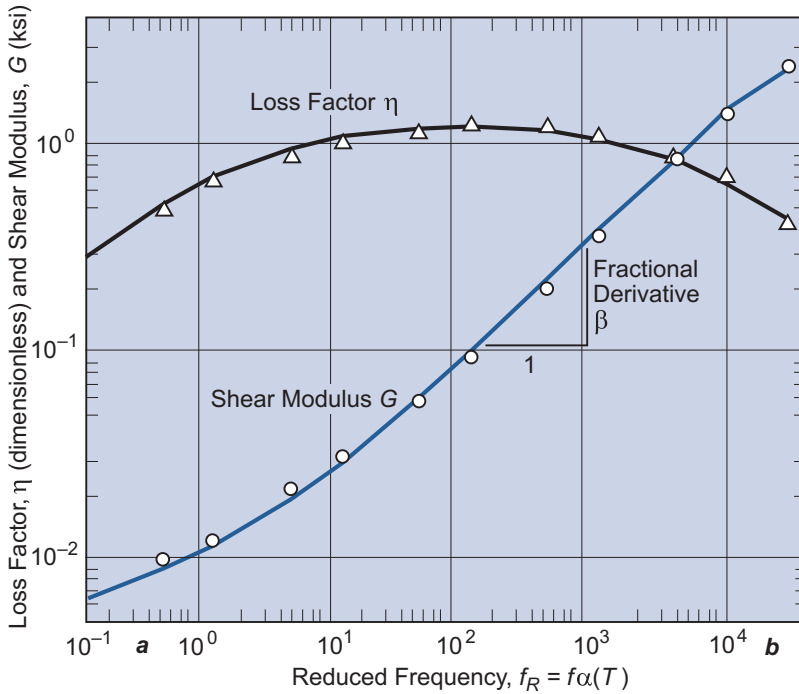


**Figure 7. Measured VEM storage modulus and loss factor as functions of reduced frequency**

Figure 9 shows the transmissibility test setup. The strut is aligned so that its tip is in a cavity of the square test mass at its exact center of gravity. The isolator’s elastic center of force passes through the apex of the V-flexure and subsequently through the test-mass center of gravity. A noncontact actuator applies a lateral disturbance force vectored through the test-mass center of gravity. The input force is measured by a quartz load cell. In such an *inertial confinement* approach, the test mass is excited entirely symmetrically, and lateral response ensues with no coupling to rotational or axial modes. Had we tried to enforce lateral motions using restraining flexures, as many isolator tests are performed, significant complicating dynamics of the restraint system would have been introduced. No parasitic dynamics appeared in our test setup. The use of a noncontact actuator also eliminated parasitic dynamics that would result from the more usual stinger test.

The opposite end of the isolator strut is clamped to a stiff, heavy base. The transmitted lateral force is measured using an average of the shear outputs of three quartz load cells. Transmissibility is then the ratio of output force to input force as the excitation is swept through frequency. The temperature of the strut was controlled to 7°C by pumping chilled fluid through tubing spirally wound around the strut.

Figure 10 compares the measured transmissibility of a JWST strut with the model prediction. The isolation achieved, even for the isolator frequency set at 2 Hz, is greater than 40 dB for most of the reaction-wheel speed range from 12 to 90 revolutions per second. Isolation is never worse than 28 dB, from 12 Hz through 1 kHz. Correspondence between measured and predicted transmissibility was excellent across three decades of frequency.

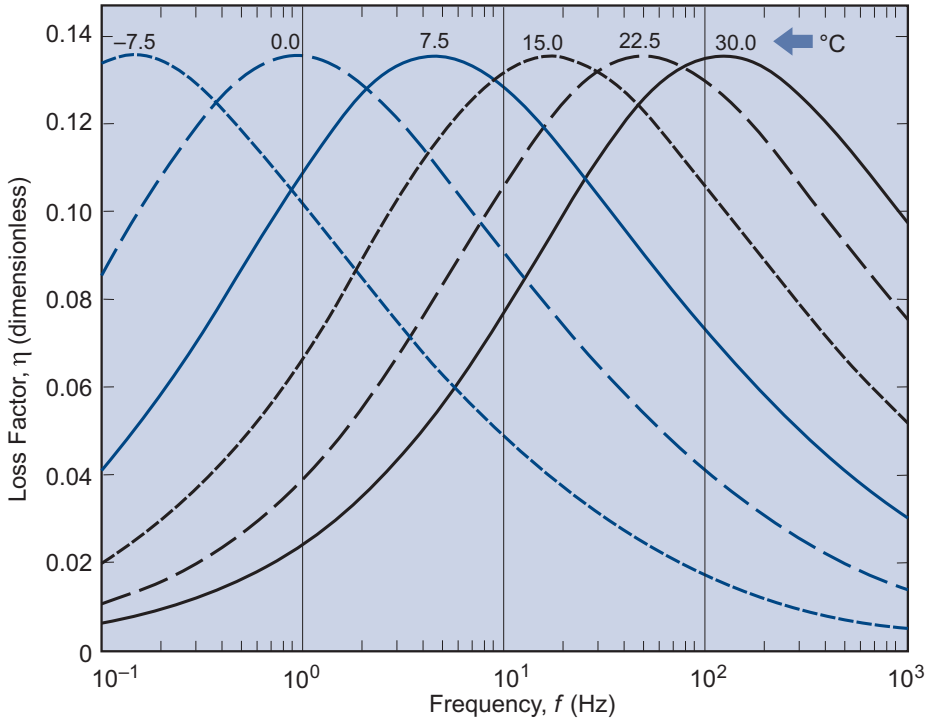


**Figure 8. Predicted loss factor in Webb telescope damped beam as function of temperature and frequency (average strut properties)**

The isolator strut system model was built using 14 simple beam elements, augmented by the closed-form complex stiffness of the damping treatment, as described previously (pages 27–31). Table 1 summarizes measured and predicted frequency and damping in the fundamental isolator mode, as well as in the first two bending modes within the isolator strut. Again, the match between analysis and test is excellent.

Transmissibility results for the SIM/STB3 struts were similar in character, albeit with a higher isolation frequency. They also provided an excellent match to model predictions. Since the entire SIM PSS will be controlled to room temperature with a stability of 1 mK, the STB3 isolator struts were tested at ambient temperatures.

## Webb Telescope Full-Scale Dynamic Simulator

To confirm the ability to achieve a 1-Hz bounce mode at 0°C, as well as to validate our understanding of the complex dynamics of a multistrut isolator, a test was devised that emulated the mass and inertia of the proposed Next Generation Space Telescope’s optical payload. The mass simulator consists of four 500-lb steel cylinders mounted on 7-ft steel tubes in a cruciform arrangement. The four isolator struts form another cruciform that is clamped to a wall by the V-flexures. The two cruciforms are connected by an octagonal steel drum, as shown in Figure 11. An approximately 30-ft-long suspension cable is attached to the exact center of gravity of the mass simulator. The cable constrains the vertical mode in the X direction but allows the Y lateral mode, the Z bounce mode, and all three rotational modes. Thus, five of the six isolator modes are measurable with this simple offload.

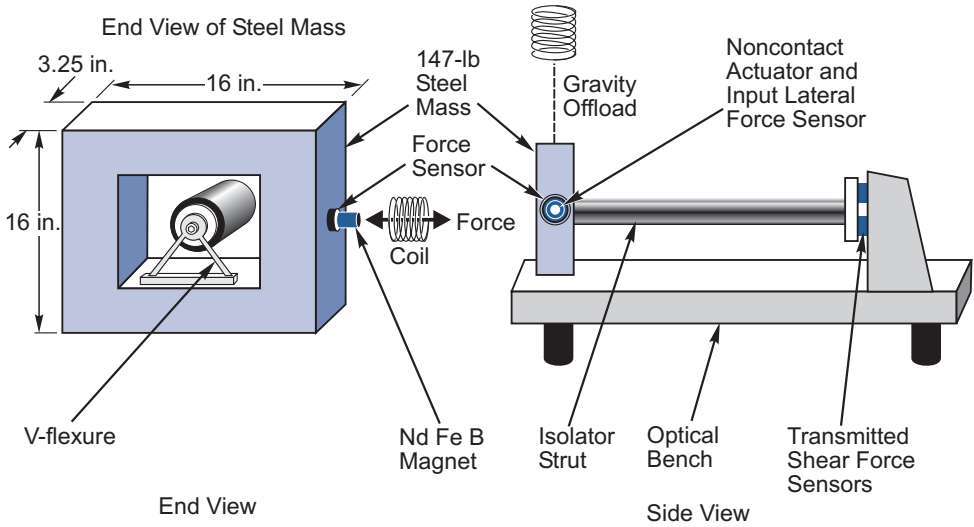


Figure 9. Unit transmissibility test setup

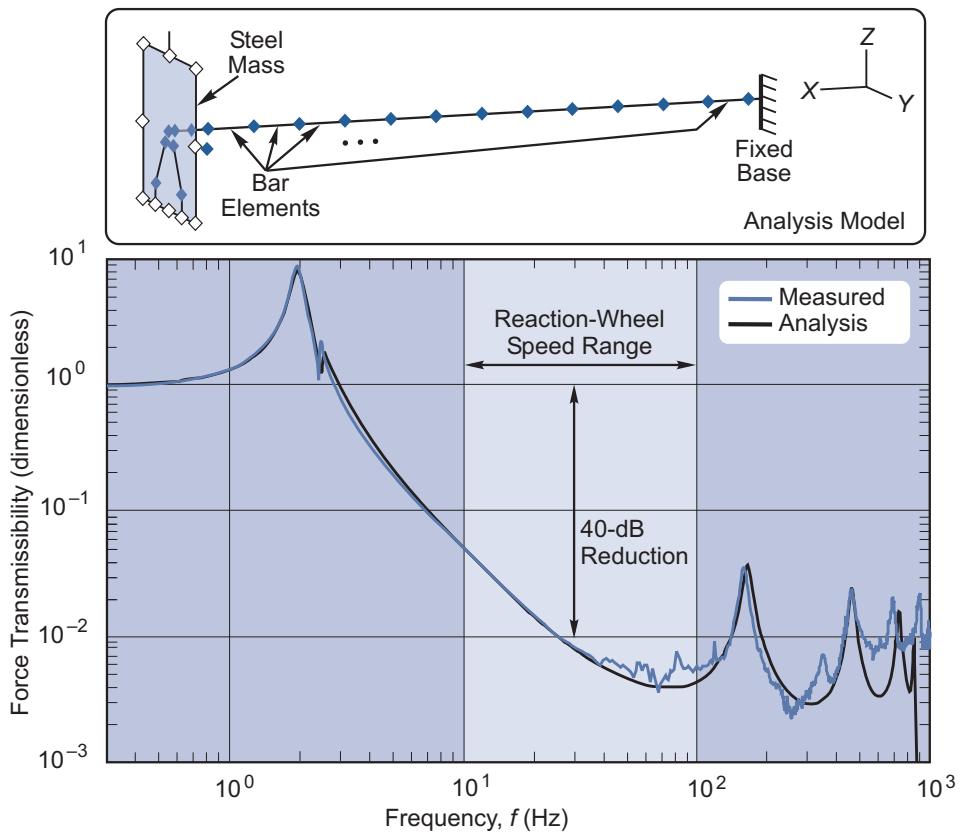


Figure 10. Unit transmissibility results for Webb telescope isolator strut 2 at 7°C

**Table 1. Test-model comparison for Webb telescope isolator strut 2 with 147-lb tip mass at 7°C**

Modal Description	Frequency (Hz)		Damping (%)	
	Test	Model	Test	Model
Fundamental bending	1.96	1.98	5.71	5.76
First bending	160.00	166.00	3.86	3.89
Second bending	461.00	464.00	3.01	2.54

All four isolator struts were wrapped with chilled tubing and multilayer insulation. Modal surveys were then performed at temperatures ranging from  $-13^{\circ}\text{C}$  to  $+23^{\circ}\text{C}$ , with frequency and damping results as shown in Figure 12. A 1-Hz bounce mode was achieved with peak damping at  $0^{\circ}\text{C}$ , as predicted. The measured trends in stiffness and damping followed those from model predictions. Frequencies increased as temperature was decreased, and damping was highest in the transition region.

Most important, the damping in all isolator modes was demonstrated at greater than 4% over a permissible operating temperature range of  $\pm 5^{\circ}\text{C}$ —sufficient to achieve the JWST isolation objectives.

### System Testbed 3 Dynamic Simulator Results

An extensive series of tests was run on STB3 to demonstrate the actual performance of the isolator operating in three dimensions between two complex flexible structures [5]. Experiments were run with the backpack isolated and also hard-mounted to the PSS. Figure 4b (page 29) shows the six brackets used to hard-mount the backpack to the PSS. When the brackets were removed, the backpack hung below the PSS on the three isolator struts, creating the isolated condition.

- Isolator modes are in the range 2.45 to 5.41 Hz.
- Backpack flexible modes are 46.7 Hz in torsion and 66.6 Hz in bending.
- PSS flexible modes are 16.0 Hz in torsion and 10.43 Hz in bending.

To replicate the reaction-wheel disturbance, a force excitation was applied directly to the floor of the backpack by the noncontact actuator, avoiding interactions between the backpack and the ground. Transfer functions were measured for excitation in each of the global X, Y, and Z axes. The transfer functions provide a measure of optical response on the payload for a unit input disturbance force. By later convolving the measured transfer functions with known disturbance models for the reaction wheels [9], optical performance can be predicted as if the reaction wheels were actually operating in the backpack.

Optical performance was measured in a pseudomanner using very-high-sensitivity (10 V/G) accelerometers. Optical path difference (OPD) is the difference in path length to a star between two arms of the interferometer as the light reaches the beam combiner. Baseline is simply the distance between the centroids of the siderostats. OPD and baseline are used to compute stellar angles. It was not possible to measure OPD optically, since STB3 had no star simulator at the time. A pseudomeasure was obtained by mounting two accelerometers each to posts on the extreme east and west siderostat pallets, as well as one accelerometer to a beam combiner, applying the formula  $\text{OPD} = (-\ddot{X}_W + \ddot{Y}_W + \ddot{X}_E + \ddot{Y}_E - 2\ddot{Y}_C)/(2\pi f)^2$ .

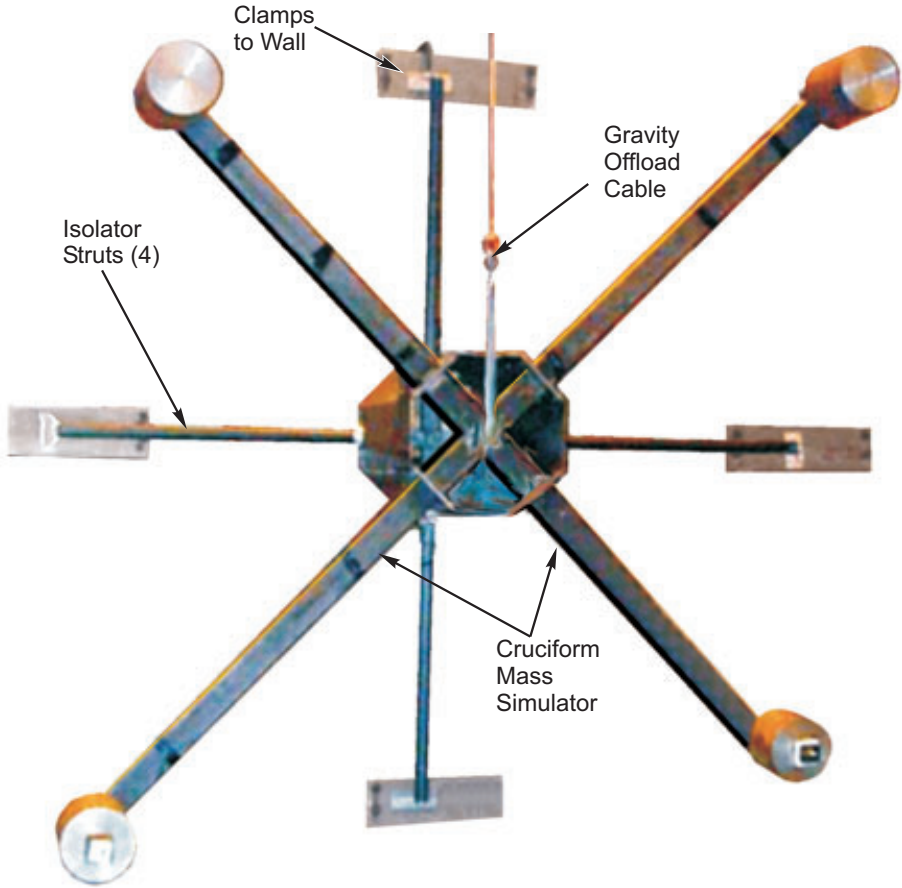


**Figure 11. Full-scale Webb telescope isolator test setup**

It was possible to measure the baseline optically using a JPL-developed beam launcher. The device bounced light between the same two posts holding the accelerometers, which also had retroreflectors mounted to them. It measured changes in the 8.5-m baseline interferometrically to a resolution of 50 pm. The baseline measurement allowed us to determine the efficacy of the pseudomeasurements. The correspondence between baseline transfer functions directly measured optically and those inferred from acceleration was remarkable, matching within 0.1 nm/Newton from 3 Hz through 300 Hz. Above 300 Hz, vibration modes in the post itself created differences. Below 3 Hz, drift in the accelerometers and/or the effects of air motions on the light beams came into play. The accelerometers were likely the major limitation below 3 Hz, since they do not measure to zero frequency, and their signal is being divided by frequency squared, which amplifies low-frequency noise.

Another effect complicating low-amplitude testing is direct acoustic transmission. When the backpack is excited, its panels vibrate, transmitting acoustic waves that are received by and excite the PSS. The transmissibility “noise floor” due to that effect was found by completely disconnecting the backpack from the PSS, instead supporting it on the floor using soft foam isolators, and measuring transfer functions to the optics mounted on the PSS. Acoustic transmission was found to be a prominent effect at the panel-mode

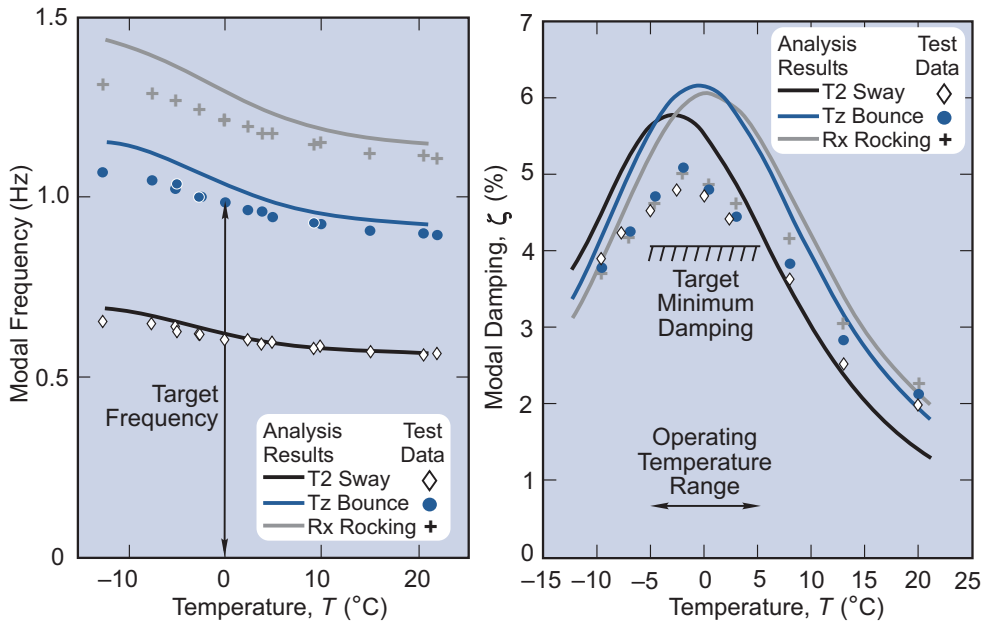


**Figure 12. Full-scale Webb telescope modal survey test results and model correlation**

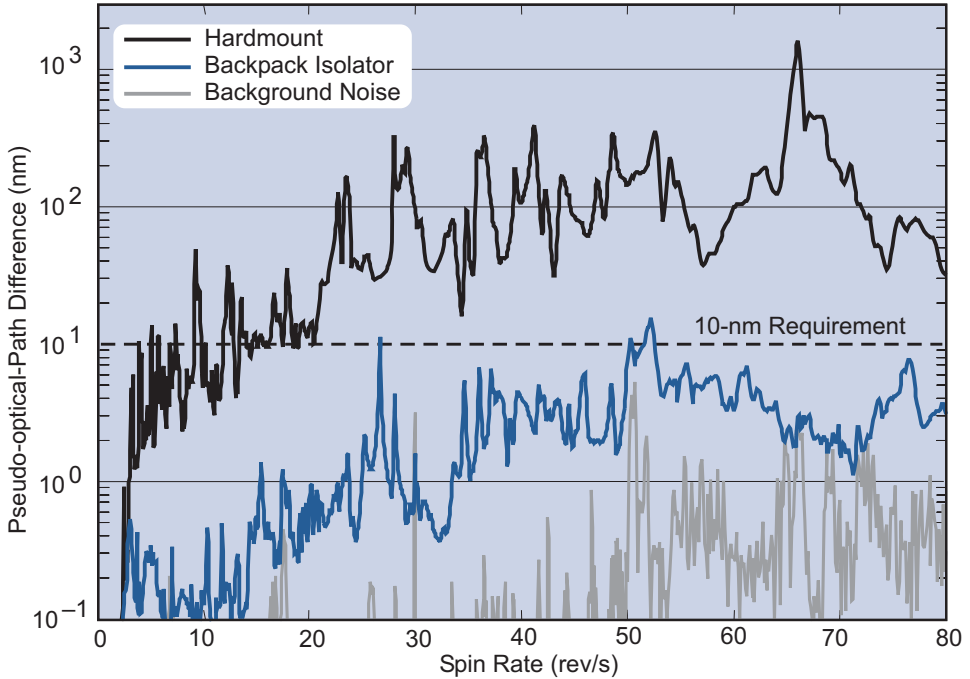
frequencies above 100 Hz. An acoustic barrier was built around the backpack to mitigate that condition, but it was not completely effective, because of penetrations as well as limitations in barrier thickness between PSS and backpack.

Figure 13 shows the pseudo-OPD measured with the acoustic barrier in place. The backpack isolator succeeds in reducing peak motions by two orders of magnitude for wheel speeds from 6 to 80 revolutions per second. The 10-nm OPD requirement is met at nearly all wheel speeds with just the single stage of full-spacecraft isolation. The acoustic noise floor was significant; it was found to obscure performance above 100 Hz when a second layer of source isolation was in place. The single-isolation-stage results were not affected severely.

## Future Applications Using Active-Structure Technology

One can imagine applications where one might wish to steer a large optical payload at a bandwidth greater than that which the spacecraft attitude-control system can provide. One example is a telescope with a very narrow field of view—say,  $2 \times 2$  arc-minutes, which must interrogate a patch that is  $1^\circ \times 1^\circ$ . An active isolator that can steer  $\pm 0.5^\circ$  could thus provide an increase of a factor of 900 in field of regard.

The beam isolator is adaptable to such applications by embedding active materials into the tubes to allow positioning of the payload by bending the struts. Full 6-degree-of-freedom motion control is possible by bending each of three struts about both axes. Rapid settling after slew can be obtained by employing piezoelectric sensor patches bonded to the struts to provide a high-sensitivity strain signal for active damping.



**Figure 13. System Testbed 3 pseudo-optical-path-difference reaction wheel jitter performance, including active optics filter**

Northrop Grumman Space Technology demonstrated such an active isolator in the mid-1990s. The Smart Structures Experimental Test Set (SSETS), shown in Figure 14, employed lead-zirconate-titanate (PZT) sensors and actuators embedded in fiberglass struts. Six local damping loops provided 20% damping of the isolator modes. A global control loop from two telescope tilt sensors to the three vertical actuators provided control authority with very high disturbance rejection.

A 2-s response time was achieved for a step tilt command, as Figure 15 shows. However, the angular range of the isolator was only a few arc-minutes, due to the low strain actuation in embedded PZTs. Using active-material technology of the 1990’s, applications would be limited by that range of motion. Such applications do exist—one example being the Terrestrial Planet Finder–Coronagraph, where the entire telescope must be pointed to an accuracy of ~1 mas to allow light from the central star to be blocked, while nearby planets can appear in the null spots in the resulting diffraction pattern.



**Figure 14. Smart Structures Experimental Test Set active beam isolator**

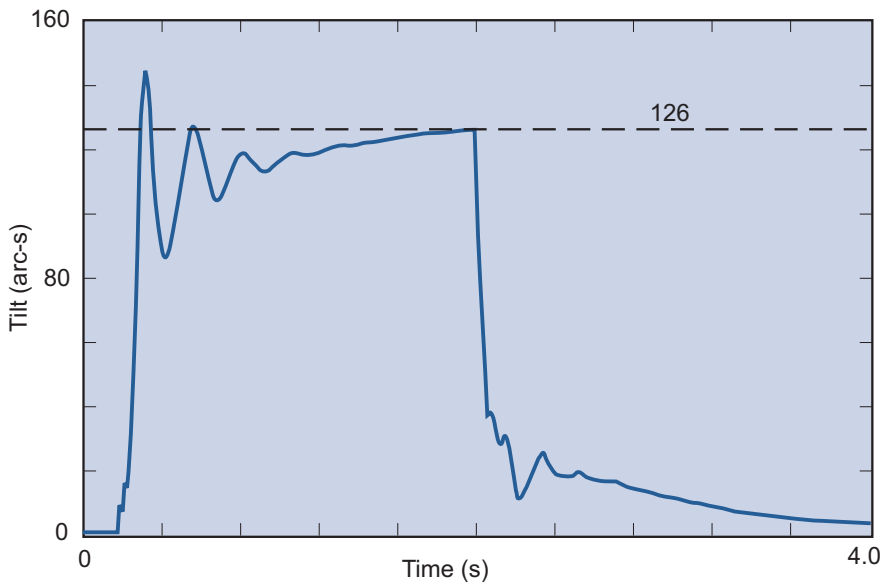


**Figure 15. Smart Structures Experimental Test Set tilt response to step command**

## Conclusions and Recommendations

The beam isolator concept has been found to be a simple, effective, and predictable solution to a number of spacecraft-isolation problems. It was a key factor in our award of the JWST contract. It packages easily, since the three or four beams lie flat between the spacecraft and payload. Parasitic dynamics are also low. An alternative isolation approach proposed for spacecraft employs six struts acting as axial flexures in a hexapod configuration. However, that approach allows for 12 cross-axis paths between the two bodies being isolated (two transverse axes on each of six struts). With the beam isolator, the only cross-axis terms are along the axial direction of each strut. The forces transmitted in that direction are small, as the V-flexure is designed to be ten times softer axially than the strut is laterally.

The demonstrated ability to predict stiffness and damping in a co-cured composite lay-up that includes a soft viscoelastic material was a significant analytical advancement. The 1-Hz isolation frequency of JWST was lower than most prior VEM applications and required low-temperature operation to achieve optimal damping. Luckily, the isolator is connected to a cryogenic payload, which enables operation at the optimal damping temperature. The tests confirmed our ability to predict performance and operate at extreme temperatures and frequencies.

Another advantage of the beam isolator is its large deflection capability in gravity, as fully demonstrated on STB3. The test of the “sacrificial” strut that survived indicates that an isolator as soft as 4 Hz could easily be tested in gravity without an offload.

One lesson learned is that demonstrating ultralow vibration response in air is difficult. The more effective the isolation, the more one must deal with direct acoustic transmission around the isolator.

## Acknowledgments

The JWST isolation development was entirely funded by a Northrop Grumman Space Technology internal research and development program before the award of the JWST contract, which is managed by the Goddard Space Flight Center. The STB3 testbed structure and isolator development was entirely funded by the Space Interferometry Mission, managed by the Jet Propulsion Laboratory.

## References

1. J. Nella et al., “JWST Observatory Architecture and Performance,” *Proc. SPIE*, Vol. 5487-26, *Astronomical Telescopes and Instrumentation*, June 2004.
2. R. Danner and S. Unwin (eds.), *Space Interferometry Mission, Taking the Measure of the Universe*, JPL 400-811, 1999.
3. A.J. Bronowicki, “Vibration Isolator for Large Space Telescopes,” *AIAA J. Spacecraft & Rockets*, to be published 2005.
4. R. Goullioud and O.S. Alvarez Salazar, “Dim Star Fringe Stabilization on the SIM Testbed 3 Using Pathlength Feed-forward of the ‘Guide’ Interferometer Optical Path,” *Proc. SPIE*, Vol. 4852-52, *Interferometry in Space*, August 2002.

5. A.J. Bronowicki, R. MacDonald, Y. Gursel, R. Goullioud, T. Neville, and D. Platus, "Dual-Stage Vibration Isolation for Optical Interferometer Missions," *Proc. SPIE*, Vol. 4852-68, *Astronomical Telescopes & Instrumentation*, pp. 753–763, 2002.
6. A.D. Nashif, D.I.G. Jones, and J.P. Henderson, *Vibration Damping*, Wiley, New York, 1985.
7. R.L. Bagley and P.J. Torvik, "Fractional Calculus—A Different Approach to the Analysis of Viscoelastically Damped Structures," *AIAA J.*, Vol. 21, No. 5, May 1983, pp. 741-748.
8. G. Kress, "Improving Single Constrained-Layer Damping Treatment by Sectioning the Constraining Layer," *The Role of Damping in Vibration & Noise Control*, ASME, DE Vol. 5, September 1987, pp. 41–48.
9. R.A. Masterson and A.J. Bronowicki, *Simplified Teldix RDR 68-4 RWA and Isolator Models*, TRWIOC M740-61, March 31, 2000.

## Author Profiles



**Allen J. Bronowicki** is a Technical Fellow at Northrop Grumman Space Technology, where he has worked for 26 years. He is currently the Integrated Modeling lead on the James Webb Space Telescope, tying together structural, optical, and thermal disciplines across several organizations. He has published numerous technical articles in the *AIAA Journal* and *Smart Materials and Structures* on topics such as structural optimization, parameter estimation, and modeling of active and passive damping materials. He holds a dozen patents in the area of vibration and shape control. He received a PhD in mechanics and structures from the University of California at Los Angeles.

[allen.bronowicki@ngc.com](mailto:allen.bronowicki@ngc.com)



**John W. Innis** is a software and electrical engineer at Northrop Grumman Space Technology, with 35 years of aerospace experience focused primarily in the area of control electronics. He has contributed his expertise to the structure-electronics integration on all of our smart structures programs since 1987. He is a recipient of the TRW Chairman's Award for Innovation. He holds an Associate of Science degree from Santa Monica City College.

[john.innis@ngc.com](mailto:john.innis@ngc.com)